Characterizing the Impact of Oligomerization on Redox Flow Cell Performance

Citation: T. A. Weiss, G. Fan, B. J. Neyhouse, E. B. Moore, A. Furst, F. R. Brushett, Batteries & Supercaps 2023, 6, e202300034.

Published Version: 10.1002/batt.202300034

Publisher: Wiley

Permanent Link: https://hdl.handle.net/1721.1/157757

Version: Final published version: final published article, as it appeared in a journal, conference proceedings, or other formally published context

Batteries & Supercaps

Research Article
doi.org/10.1002/batt.202300034

Chemistry Europe
European Chemical Societies Publishing

www.batteries-supercaps.org

Special Collection

Characterizing the Impact of Oligomerization on Redox Flow Cell Performance

Trent A. Weiss,[a] Gang Fan,[a] Bertrand J. Neyhouse,[a, b] Evan B. Moore,[a] Ariel Furst,[a] and Fikile R. Brushett*[a, b]

Redox flow batteries (RFBs) are hindered by complex failure modes, particularly crossover through the membrane, resulting in capacity fade and reduced cycling efficiencies. Redox-active oligomers (RAOs) have recently been proposed for mitigating this phenomenon while maintaining sufficient transport properties; however, to date, few studies have quantified how the chemical and electrochemical properties of RAOs influence their performance in redox flow cells. Here, we demonstrate that oligomeric derivatives of 2,2,6,6-tetramethylpiperidine 1-oxyl (TEMPO) exhibit lower diffusivities than the monomeric species but retain facile charge transfer characteristics. The size-dependent variations in mass transport rates directly translate to differences in flow cell polarization and symmetric cycling performance. Post-mortem analyses reveal that oligomerization does not meaningfully alter decay processes as evinced by similar capacity fade across all species. Broadly, these findings corroborate and extend upon previously developed relationships between molecular size, electrochemical properties, and flow cell performance.

Introduction

Electrochemical energy storage technologies are key enablers of renewable electricity resources (wind, solar),[1] and redox flow batteries (RFBs) show particular promise for longer-duration, grid-scale applications, as the system architecture provides inherent scalability, design flexibility, and simplified maintenance.[2] Still, state-of-the-art vanadium RFBs are hampered by high capital costs,[3] motivating the exploration of new redox electrolytes (i.e., redox couples, additives, supporting salts, solvents)[4] and membranes/separators[5] that may offer pathways to lower production costs and enhanced battery performance. While many of these alternative materials positively impact upfront techno-economic metrics, they also display more varied and complex failure modes in the longer-term, including molecular decay[6] and crossover,[7] which complicate their potential deployment. Specifically, the crossover of redox species through semi-permeable membranes/separators that separate the positive and negative electrolytes imposes losses in capacity between charge and discharge half-cycles (i.e., lower coulombic efficiency) and between full charge/discharge cycles (i.e., capacity fade).

Crossover presents a significant challenge for materials development, as the membrane/separator is simultaneously responsible for preventing undesired redox species transport while facilitating ionic conductivity and mitigating ohmic losses.[8] This is especially salient for nonaqueous RFBs, as current membrane/separator options for these devices are less selective and less conductive than their aqueous counterparts.[5,9] In general, separation can be achieved through the use of charge-selective ion-exchange membranes and/or size-selective nanoporous separators, which both require coordinated design of the active species and the membrane/separator. Of these two options, size selectivity is particularly intriguing, as it promises to minimize crossover without compromising supporting electrolyte transport (conductivity) while potentially using inexpensive porous materials, provided suitable redox couples and associated electrolyte formulations can be identified.[10] Enabling this approach requires the advent of redox-active molecules that are large enough to be rejected by pores of nano- to micrometric diameter but retain efficacious electrochemical/transport characteristics and atom-economy. To this end, there is growing interest in the integration of monomeric redox species into macromolecular scaffolds to form redox-active oligomers (RAOs),[11] polymers (RAPs),[12] and colloids (RACs);[13] the increased solvated radius of such molecules (ca. 1 nm–1 μm) can facilitate size-sieving through nanoporous and microporous separators. Previous work has encompassed a range of molecular redox units–2,2,6,6-tetramethylpiperidine 1-oxyl (TEMPO), ferrocene, viologen, cyclopropenium–tethered to numerous oligomeric and polymeric backbones, including functionalized polystyrene, polyethylene glycol, and alkylamines, providing a broad range of

[a] T. A. Weiss, Dr. G. Fan, Dr. B. J. Neyhouse, E. B. Moore, Prof. A. Furst, Prof. F. R. Brushett
Department of Chemical Engineering
Massachusetts Institute of Technology
Cambridge, MA 02139 (USA)

[b] Dr. B. J. Neyhouse, Prof. F. R. Brushett
Joint Center for Energy Storage Research
Massachusetts Institute of Technology
Cambridge, MA 02139 (USA)
E-mail: brushett@mit.edu

Supporting information for this article is available on the WWW under https://doi.org/10.1002/batt.202300034

An invited contribution to a Special Collection on Organic Batteries

molecular engineering strategies for active material design.[11,14–18]

Despite their improved crossover resistance, the increased solvated radius of macromolecular species hinders mass transport, as bulkier species diffuse more slowly through the electrolyte.[19–21] This results in lower limiting currents and increased overpotentials, reducing power densities, accessible capacity, and cycling efficiencies for larger redox species. Further, at high active species concentrations, RAP- and RAC-containing electrolytes exhibit high viscosity and non-Newtonian rheology,[22,23] which result in significant pumping losses and other device engineering challenges. Given the complexities presented by redox electrolytes with polymeric and colloidal components, RAOs may present an effective compromise for these competing design considerations, as the molecular weights only marginally exceed those of their respective monomers while sufficiently mitigating crossover when paired with nanoporous membranes (e.g., polymers of intrinsic microporosity,[24,25] engineered cellulose[17]). While there has been considerable effort to discover, synthesize, and characterize new materials,[11,14,15,26] fewer studies have focused on investigating the electrochemical performance of these materials in redox flow cells. Such studies can provide a deeper understanding of the factors that influence performance tradeoffs, enabling molecular design and cell engineering campaigns. However, this approach also requires time- and materials-intensive testing in redox flow cells, necessitating small-volume cell formats, facile synthesis routes, and model redox couples to assess RAOs under conditions that resemble practical embodiments.

In this work, we systematically evaluate a series of small oligomers, from monomers to tetramers, based on a well-defined redox couple (TEMPO/TEMPO$^+$), with a focus on how increasing molecular size impacts flow cell performance. First, we apply voltammetric methods–cyclic voltammetry (CV) on stationary and rotating disk electrodes–to characterize electrochemical kinetics and diffusivity of the different forms of TEMPO in the reduced and oxidized states. We find a nonobvious relationship between diffusivity and oligomer size, and perform metadynamics simulations to aid in the interpretation of this trend. Using symmetric redox flow cells at 100 mM TEMPO moiety concentrations and 50% state of charge (SoC), we then characterize cell performance through polarization and electrochemical impedance spectroscopy (EIS). Subsequently, we perform cell cycling experiments with each oligomer to assess species stability and accessible capacity as a function of size, finding changing mass transfer limitations that scale with molecular diffusion, consistent with the polarization/EIS behavior. Furthermore, we observe minimal variations in capacity fade rates, which suggests that, at least for this set of compounds, the oligomer backbone does not appreciably influence chemical decay pathways. This is corroborated by post-mortem electrochemical analyses of the cycled redox electrolyte. Overall, this work shows that, while the integration of redox couples into oligomeric structures can alter transport properties, there is a clear connection between molecular properties and cell performance, further informing design strategies for emerging RFBs.

Results and Discussion

To evaluate how molecular size impacts the electrochemical performance of RAOs, we selected TEMPO and its polyethylene glycol (PEG) oligomeric variants–a dimer, trimer, and tetramer–as model compounds for electroanalytical and flow cell testing. TEMPO is a well-known redox couple featuring fast electrochemical kinetics, relatively stable cycling, and facile synthetic functionalization, making it suitable for assessing mass transport aspects without convolution from other complicating factors.[27,28] Similarly, PEG chains are easily functionalized and typically impart heightened stability and solubility in non-aqueous electrolytes.[29,30] Details of the synthetic procedure for functionalization of the PEG backbones into RAOs can be found in the Supporting Information (SI).[14] In brief, we tosylated the PEG precursors before substituting 4-hydroxy-TEMPO onto the oligomer backbone using sodium hydride under reflux conditions (Scheme 1); the products were obtained in 45.8–49.5% yield and 90–95% purity with decreasing purity and yield correlating with increasing oligomer size as determined by nuclear magnetic resonance (NMR) spectroscopy, high-performance liquid chromatography (HPLC), and mass spectrometry (MS) (Figures S1–S4). While the synthesized dimer was a solid, the trimer and tetramer variants were viscous oils (Figure S4). To characterize the oxidized state and deterministically prepare 50% SoC electrolytes for symmetric flow cell testing, the reduced forms of the redox-active oligomers were oxidized via a nitrosonium tetrafluoroborate salt[31] in acetonitrile with high yield ($>$98%) and SoC ($>$99%) (Section S2).

Electroanalytical measurements and molecular characterization

We employed CV to investigate the influence of oligomerization on the chemical and electrochemical reversibility of each compound and thus any changes in the nature of the charge transfer process. These experiments were conducted on a glassy carbon working electrode with solutions containing 1 mM of the monomer or the oligomers and an excess of supporting salt. Note that the active species concentrations refer to that of the molecule, such that the total TEMPO moiety concentrations of the dimer, trimer, and tetramer are 2 mM, 3 mM, and 4 mM, respectively. Additional experimental details can be found in the Experimental Section. The resulting voltammograms (Figure 1) demonstrate that tethering the TEMPO moiety to a PEG backbone leaves the redox potential unchanged ($E_{1/2}$ between 0.280–0.290 V vs. Fc/Fc$^+$ for all compounds), suggesting limited electron-donating (or withdrawing) effects from the oxygen in the backbone on the electronic structure of the free radical.[30] In all oligomeric variants over the range of CV conditions considered in this work, the peak splitting (ΔE_p) and width at half max ($E_{p/2}$) at 26 °C (the temperature at which the

Research Article
doi.org/10.1002/batt.202300034
Chemistry Europe
European Chemical Societies Publishing

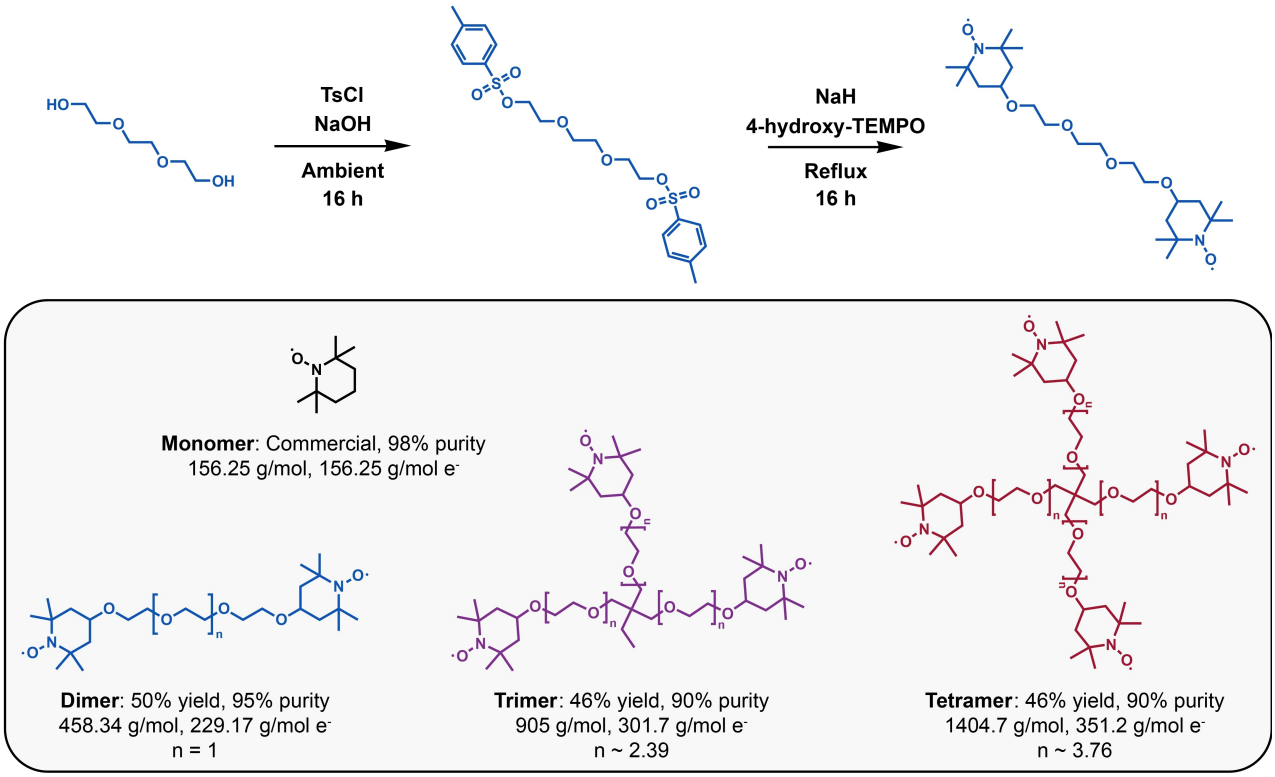

Scheme 1. Synthesis of the TEMPO-PEG dimer (top) as a representative example as well as structures, yields, purities, and linker lengths (n) of the oligomers (bottom). TsCl is *p*-toluenesulfonyl chloride, NaOH is sodium hydroxide, and NaH is sodium hydride in the synthetic pathway shown.

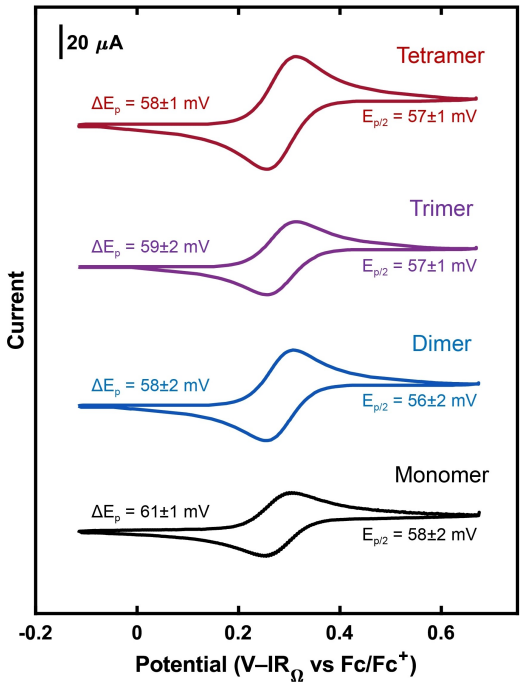

Figure 1. IR-corrected cyclic voltammograms of the monomer and oligomers with 1 mM active species and 0.5 M $TEABF_4$ in acetonitrile using a 3-mm glassy carbon working electrode, a platinum wire counter electrode, and a Ag/Ag^+ reference electrode at a 50 $mV\,s^{-1}$ scan rate. Potentials are referenced against the Fc/Fc^+ redox couple. ΔE_p denotes the difference in peak potential and $E_{p/2}$ signifies the width at half max of the forward scan. Data for each measurement was collected in duplicate.

voltammetry experiments were conducted at) are both ca. 57 mV, which is indicative of a chemically and electrochemically reversible, sequential electron transfer process (Tables S2 and S3).[32,33] Note that, if electron transfer was not sequential, these values would be noticeably lower (Section S3)–specifically, they would be inversely related to the number of active sites per molecule. Additionally, the presence of a single, reversible peak in both the oxidative and reductive sweeps suggests that the redox event at each active site is electronically isolated from the other sites on the molecule.[14,15] Taken together, oligomerization appears to preserve the facile electrochemical kinetics afforded by the TEMPO monomer and does not seem to measurably disrupt its chemical or electrochemical reversibility across the experimental conditions tested.

Next, we sought to understand the influence of oligomerization on the mass transport properties of these molecules. The electrochemical reversibility of these electron transfer processes affords use of the Randles-Ševčík equation for quantifying oligomer diffusion coefficients according to the following relationship [Equation (1)]:[33]

$$I_p = \pm 0.4463 \left(\frac{F^3}{RT}\right)^{\frac{1}{2}} n^{\frac{3}{2}} A D^{\frac{1}{2}} C \upsilon^{\frac{1}{2}} \quad (1)$$

where I_p (A) is the peak current, F (96,485 $C\,mol^{-1}$) is the Faraday constant, R (8.314 $J\,mol^{-1}\,K^{-1}$) is the universal gas constant, T (K) is the absolute temperature, n (–) is the number of electrons transferred, A (cm^2) is the geometric area of the electrode, D

Research Article
doi.org/10.1002/batt.202300034
Chemistry Europe
European Chemical Societies Publishing

($cm^2 s^{-1}$) is the diffusion coefficient, C ($mol\,cm^{-3}$) is the concentration of the redox-active moiety, and v ($V\,s^{-1}$) is the scan rate. This interpretation of the variables n and C is in accordance with Flanagan et al., who state that voltammetric waves for molecules with multiple, noninteracting redox centers should have a shape matching that of a single center with a current magnitude corresponding to the total number of centers.[34] Therefore, in the Randles-Ševčík analysis presented here, n represents the total number of electrons transferred at a single site – $n=1$ in this instance – and C represents the total charge concentration utilized, namely the active species concentration multiplied by the number of redox-active centers. This distinction is relevant as n and C exhibit distinct scaling – the exponents are 3/2 and 1, respectively – such that improper delineation and accounting of these values leads to incorrect diffusion coefficients. Figure 2(a) illustrates a representative sample of the CV profiles for scan rates between 10–500 $mV\,s^{-1}$. Plotting the peak currents against the square root of the scan rates in Figure 2(b) enables extraction of the diffusion coefficients as reported in Figure 3 (vide infra). Note that the magnitude of the slopes in Figure 2(b) do not necessarily follow the trend of the diffusion coefficients due to the convoluting effect of the changing total charge concentration.

Given the transient nature of the Randles-Ševčík analysis, we subsequently sought to confirm the calculated diffusion coefficients with Levich analysis, a complimentary electrochemical technique that utilizes a rotating disk electrode to generate steady-state limiting currents as defined in Equation (2).[33]

$$I_L = \pm 0.62nFAD^{\frac{2}{3}}\omega^{\frac{1}{2}}\nu^{-\frac{1}{6}}C \quad (2)$$

I_L (A) is the plateau current, ω ($rad\,s^{-1}$) is the rotation rate, and ν ($cm^2 s^{-1}$) is the kinematic viscosity. Note that the exponential scaling of n and C are identical (i.e., the exponents are both 1), meaning careful definition of the concentration as either that of the molecule or that of the redox center is inconsequential and, importantly, independent of the electron transfer mode (i.e., concerted or sequential). Figure 2(c) illustrates representative voltammetric profiles for the dimer on a rotating disk electrode at rotation rates between 100–2500 rotations per minute (rpm). The diffusion coefficients are determined by plotting the limiting currents against the square root of the rotation rates as shown in Figure 2(d). Again,

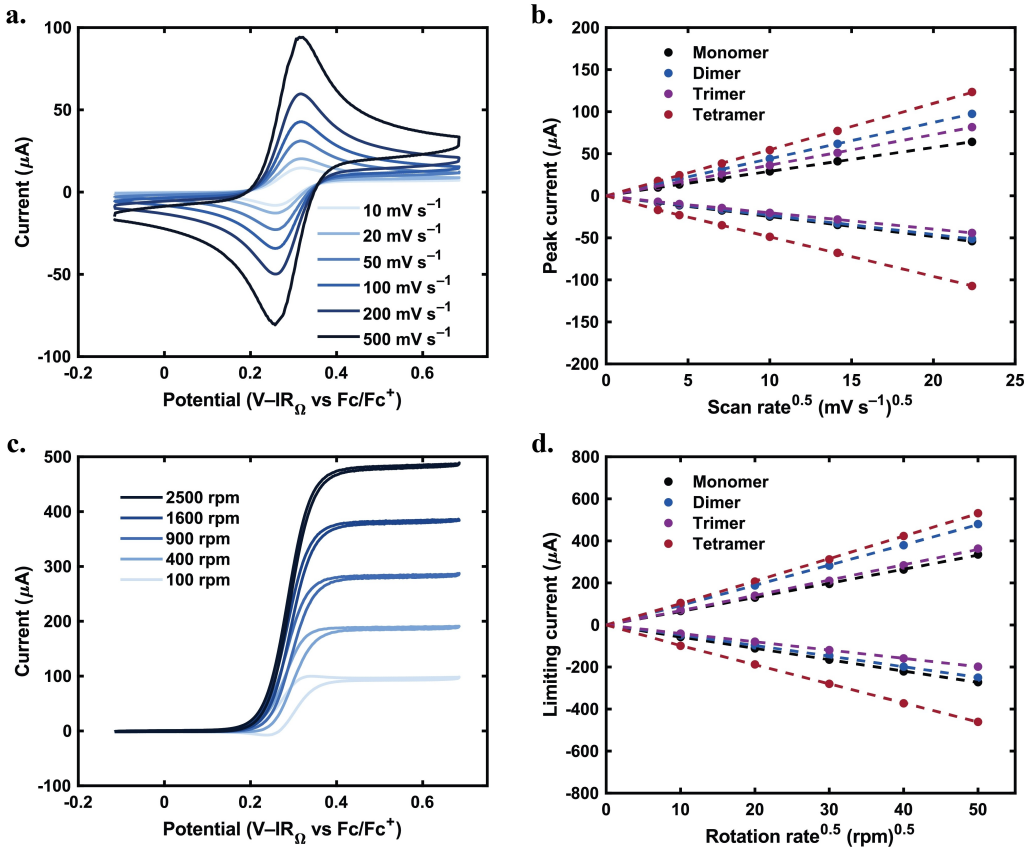

Figure 2. a) IR-corrected cyclic voltammograms of the dimer (1 mM) with 0.5 M $TEABF_4$ in acetonitrile using a 3-mm glassy carbon working electrode, a platinum wire counter electrode, and a Ag/Ag^+ reference electrode at varying scan rates. b) Peak currents for the monomer and oligomers plotted against the square root of the scan rate; positive currents represent the reduced species whereas negative currents represent the oxidized species. Dashed lines represent the results of linear regression ($R^2 > 0.999$ for all samples). c) IR-corrected cyclic voltammograms of the dimer (1 mM) with 0.5 M $TEABF_4$ in acetonitrile using a 5-mm glassy carbon rotating disk electrode taken at 10 $mV\,s^{-1}$ with the same counter and reference as in (a). d) Plateau currents for the monomer and oligomers plotted against the square root of the rotation rate. Dashed lines represent the results of linear regression ($R^2 > 0.999$ for all samples). All potentials are referenced against the Fc/Fc^+ redox couple. Data for each measurement was collected in duplicate.

Research Article
doi.org/10.1002/batt.202300034
Chemistry Europe
European Chemical Societies Publishing

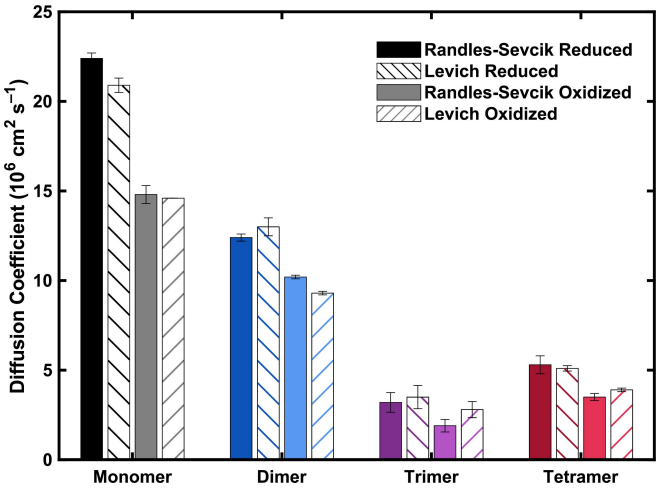

Figure 3. Calculated diffusion coefficients for the monomer and oligomers, in their reduced and oxidized forms, with 0.5 M $TEABF_4$ in acetonitrile using the Randles-Ševčík and Levich methods. Data for each measurement was collected in duplicate, with error bars representing a single standard deviation based on these measurements.

convolution of the total charge concentration and diffusion coefficients in the measured currents obfuscates direct comparisons between the magnitude of the slopes and relative rates of molecular diffusion. Figure 3 compares the diffusion coefficient values extracted from the Randles-Ševčík and Levich analyses–there is good agreement between the two. Considering the Levich scaling is independent of the nature of electron transfer, this consistency between methods offers additional verification that electron transfer occurs sequentially for these RAOs.

In evaluating the diffusion coefficients, we first note that those for the monomer are relatively consistent with those reported in prior literature for acetonitrile-based electrolytes, in which calculated diffusion coefficients range from ca. 10–30×10^{-6} cm^2 s^{-1} depending on the supporting salt and concentration utilized.[30,35,36] Comparison between the reduced and oxidized forms of the oligomeric variants demonstrates a ca. 40% increase in the diffusion coefficient for the reduced species over that of the oxidized species, which is consistent with prior RAO studies.[15] We tentatively ascribe this difference to the presence of a larger and more strongly bound solvation shell around the oxidized species due to the localized charge on the TEMPO moiety.[37] Additionally, there is a clear trend in which the diffusion coefficients for the reduced and oxidized species decrease with increasing molecular size, from monomer to tetramer, although it is disrupted by the trimer. Notably, this pattern persists even though the linker length in the PEG backbone increases with oligomer size (Scheme 1 and Section S1) due to precursor availability, where the average number of repeat units is 1, 2.4, and 3.8 for the dimer, trimer, and tetramer, respectively.

We hypothesize that there are likely multiple features that contribute to this trend in diffusivity, including the flexibility of the oligomeric arms for each species, charge distribution across each of the oligomers, and symmetry of the resulting solvation shell.[38–41] With reference to the first feature, we posit that the PEG backbone could impart additional flexibility to the tetramer as compared to the trimer due to their respective linker lengths such that the tetramer may, on average, sample conformational states smaller than the trimer. One proxy for polymer flexibility employed in polymer segment models is the Kuhn length–the effective length of a polymer segment that represents behavior of a Gaussian random coil.[42] For polyethylene glycol, the Kuhn length varies between 0.34–1.1 nm in solvents that have similar dielectric constants as acetonitrile such as acetone and dimethyl sulfoxide, which is equivalent to approximately one to four monomeric units.[43] As the tetramer has more repeat units, this suggests that it may be relatively flexible while the trimer is more rigid, such that the sizes in solution are comparable.

To investigate this further, we employed the Conformer-Rotamer Ensemble Sampling Tool (CREST), a semiempirical quantum chemical tool that employs a combination of metadynamics and molecular dynamics to sample the potential energy surface of the molecule and return optimal molecular conformations.[44,45] We first generated representative structures of each of the oligomers in Avogadro (see Figure S11), which we utilized as inputs to CREST. Additional details can be found in the Experimental Section. To assess the relative sizes of the optimal conformation for each oligomer, we employed the radius of gyration, which represents the average distance of atoms in a molecule from its center of mass.[42] In their lowest energy conformation in vacuum, the approximate radius of gyration for the dimer (4.1 Å), trimer (5.5 Å), and tetramer (6.1 Å) are much smaller than the respective fully stretched oligomers, owing to the high degree of flexibility imparted by the PEG backbone chains (see Section S5). While this trend does not wholly align with that of the diffusivities found experimentally, we highlight that the results mentioned above are that of simulations and are meant to be qualitative demonstrations that can partly facilitate explanation of the diffusivity trend found. Specifically, we posit that the close proximity of the pure oligomer sizes found here in conjunction with solvation shell effects could reasonably recreate the trends found experimentally. Though we have also explored implicit solvent simulations in CREST, we question the accuracy of these results as discussed in Section S5. Instead, we recommend that explicit solvent molecular dynamics simulations be performed to further elucidate the role of solvation on solution structuring of the molecules studied herein. We underscore that the experimental and computational findings in this study highlight the complexities associated with molecular engineering, and we encourage additional investigation in this area to clarify relationships between molecular structures and observed properties.

Nevertheless, we find that the oligomers synthesized here feature diffusivities that are in the upper echelon of RAOs studied in acetonitrile, where diffusivities range from 0.5–10×10^{-6} cm^2 s^{-1} for molecules containing between two and four active sites.[11,14,15] Additionally, the near order of magnitude decrease in diffusion coefficients for the oligomers as compared to the monomer is consistent with prior work. Ultimately, the findings discussed thus far demonstrate that oligomerization of TEMPO using a PEG backbone maintains the fast kinetics

Research Article
doi.org/10.1002/batt.202300034

afforded by the monomer as well as reasonable mass transport rates that are desirable for application in nonaqueous RFBs.[46]

Flow cell testing

Though ex situ characterization of kinetic and mass transport properties of the different RAOs offers foundational insight, flow cell analyses are necessary to explore how these properties impact cell performance under reasonably well-controlled conditions that more closely resemble practical formats. To this end, we assembled small-scale redox flow cells (2.55 cm^2 geometric area) with SGL 29AA carbon paper electrodes and a non-selective, microporous Daramic separator to characterize polarization, impedance, and cycling characteristics as a function of electrolyte composition. Additional details of the cell build can be found in the Experimental Section. The data was collected in a symmetric cell configuration, where electrolytes were deterministically prepared at 50% SoC to ascertain resistive contributions to cell polarization as well as species decay rates during galvanostatic cycling. Equal charge concentrations of 100 mM TEMPO moiety were employed for all species, corresponding to active species concentrations of 50 mM, 33.3 mM, and 25 mM for the dimer, trimer, and tetramer, respectively. Balancing the total number of equivalent redox-active sites facilitates a more direct assessment of the impact of oligomerization on mass transport and accessible capacities, as the theoretical capacity for all electrolytes is identical. We note that the conditions employed here are not optimized for high performance but rather are selected for facile comparisons. For example, the active species concentrations selected are likely too low for cost-effective RFB operation; however, operation at low concentrations increases mass transfer resistance, limits any effects larger species may have on solution viscosity, and ensures that the species are soluble across the conditions we studied.[47] Additionally, the electrodes chosen were used as-received; however pre-treatments (e.g., heat-treatment) would likely increase the electrochemically active surface area and further improve mass transport characteristics.[48] While exploration of these effects was not included in this report due to limited materials availability, future investigations will be needed to improve synthesis scales and yields to enable such detailed, multimodal studies.

We began our flow cell investigation with EIS about the open-circuit potential and polarization measurements to validate the relationship between changing diffusion coefficients and mass transport characteristics in a flow cell. Nyquist plots, generated from the impedance analysis and shown in Figures 4(a) and S13, demonstrate minimal changes in the high frequency intercept, representative of the area-specific ohmic resistance (ASR_Ω), indicating that the independent cell builds between oligomers were sufficiently consistent, as solution conductivity should not be significantly altered between species due to the presence of excess supporting salt (0.5 M $TEABF_4$). In order to enable more quantitative comparisons, a simple equivalent circuit model – here, a modified Randles circuit commonly employed for symmetric RFB systems – was fitted to the data to extract charge transfer and mass transport resistances (solid lines in Figure 4a). This model applies the typical Randles circuit, which comprises an ohmic resistance (R_Ω) in series with a reaction consisting of a diffusion-controlled charge transfer process in parallel with a double-layer capacitance, and adapts it to match RFB operation. We represent the charge transfer process as a resistor (R_{CT}) in series with a finite-length Warburg element (W_δ) that describes the convection-controlled diffusive boundary layer.[49] The double-layer capacitance is implemented as a constant phase element (CPE) to account for nonidealities in

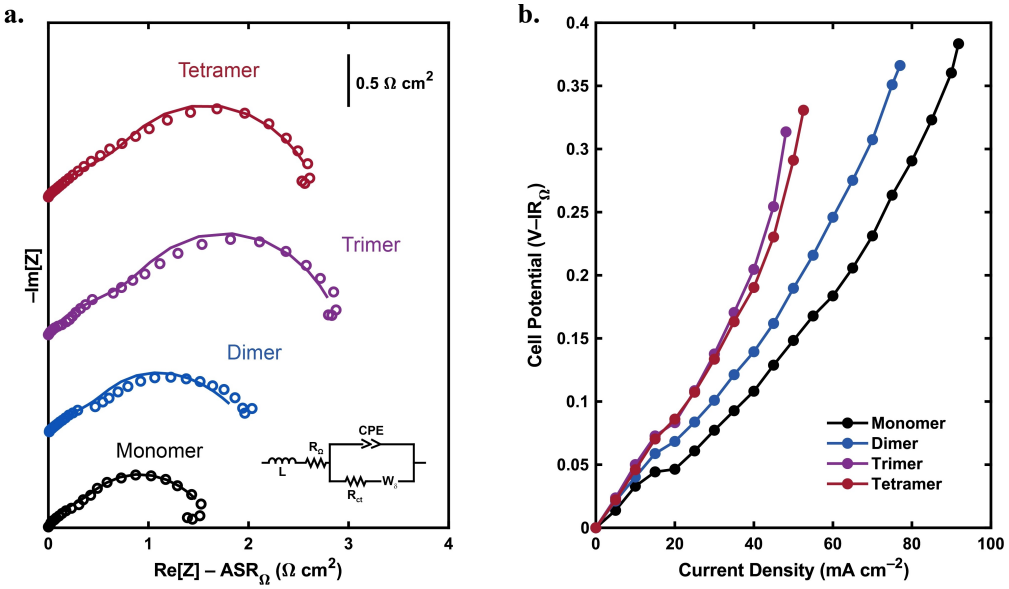

Figure 4. Symmetric cell performance at 10 mL min^{-1} flowrate and 100 mM total charge concentration deterministically prepared at 50% SoC with 0.5 M $TEABF_4$ in acetonitrile. a) Nyquist plots for the monomer and oligomers. Solid lines represent the best fit values for the equivalent circuit model (inset). b) IR-corrected polarization curves for the monomer and oligomers. Data for each point was averaged over the last 30 s of each current step.

Research Article
doi.org/10.1002/batt.202300034
Chemistry Europe
European Chemical Societies Publishing

the electrode structure.[50] Finally, we account for lead resistance by adding an inductor (L) to the front of the circuit. The values from the circuit model fitting were converted to be area-specific quantities using the geometric area of the electrode. As shown in Table S6, the increase in mass transport area-specific resistance (ASR_{MT}) in relation to the degree of oligomerization aligns with trends observed in the species diffusion coefficients (see Figure 3). As mass transport is a combination of both convection and diffusion – and superficial electrolyte velocities are consistent through identical porous electrodes across all experiments – deviations in mass transport resistance can be attributed solely to differences in diffusive transport. Though difficult to distinguish, the partial semicircle at intermediate frequencies is representative of the charge transfer resistance and double-layer capacitance, which are both relatively unchanged with respect to the oligomeric size and comparatively small in relation to the total area-specific resistance of the cell (see Table S6), corroborating the facile kinetics observed for all species. Furthermore, the electron transfer rate constants evaluated from the fitted charge-transfer resistance were found to be similar to those reported in literature (Section S6), supporting the circuit model and fitting procedure applied to the data. Polarization measurements, shown in Figure 4(b), further confirm the symmetric cell behavior suggested by the impedance analyses. As these measurements have been ohmically-corrected using the high-frequency resistance ("IR_Ω-corrected"), the potential required to maintain a given current density should primarily be influenced by kinetic and mass transport resistances as well as any distributed ohmic resistances in the porous electrodes. The trend of greater overpotentials at a given current density, a consequence of diminished mass transport, follows the same trends with the degree of oligomerization presented in all of the preceding analyses.

We subsequently performed galvanostatic cell cycling to compare accessible capacities for each oligomeric variant with the results from EIS and polarization. Electrolytes were subjected to 100 cycles at 10 mA cm^{-2} with voltage cutoffs at ±0.5 V, the results of which are presented in Figure 5. While the monomer is able to achieve close to the theoretical capacity (26.8 mAh), accessible capacities are reduced for the oligomeric variants, again in the expected order, a trend which manifests in the cycling duration for each species. To facilitate stability comparisons between the different species, we normalize by the initial capacity and report the data both by time and by cycle number (Figure S15) to ascertain whether or not the oligomeric scaffold influences the chemical stability of the species – the steric bulk could, in principle, provide protection from decay pathways but could also provide additional sites for reactive decomposition.[51] We note that capacity normalization is not a comprehensive representation of comparative stability and that the differences in accessed capacity and accessed SoC across the molecules tested could impact the relative decay rates.[52] We find that the decay rates (ca. 2% per day) observed here are on par or lower than those reported in prior literature,[30,53] although this may be due in part to differences in experimental conditions, electrochemical testbeds, and electrolyte compositions that could influence such measurements.[54] Ultimately, the decay rates do not demonstrate any significant trends that would evince a relationship between common pathways and species identity – that is, it appears that the presence of the oligomeric backbone does not influence the dominant decay pathway under the tested experimental conditions. Therefore, we sought to further characterize the decayed electrolytes via voltammetry to offer complementary information to that provided by cell cycling.

Post cycling electrochemical analysis

To better understand the causes of the capacity fade, we conducted post mortem analyses to generate complementary information to that provided above. Both microelectrode and macroelectrode voltammetry were employed to assess final SoCs as well as to elucidate any new redox events within the electrochemical window of interest that might indicate the presence of new electroactive species. Solutions were charac-

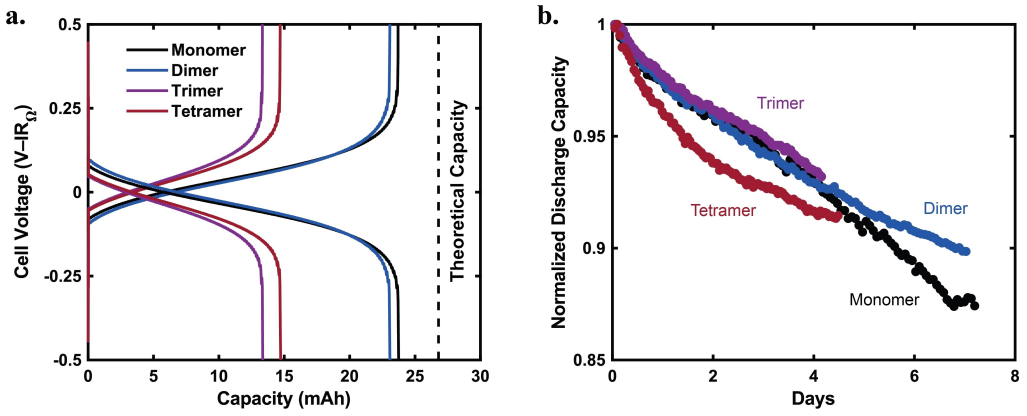

Figure 5. Symmetric cell cycling at 10 mA cm^{-2} and 10 mL min^{-1} for 100 cycles at 100 mM total charge concentration deterministically prepared at 50% SoC with 0.5 M $TEABF_4$ in acetonitrile. a) IR-corrected charge and discharge profiles for the monomer and oligomers plotted for the second cycle. b) Discharge capacities for the monomer and oligomers plotted temporally and normalized against the first cycle.

Research Article
doi.org/10.1002/batt.202300034
Chemistry Europe
European Chemical Societies Publishing

terized immediately after the cycling protocol was completed by mixing the two cell compartments together; we do not expect significant compositional differences between the two compartments due to the symmetric nature of the cell.

Microelectrodes offer large diffusion boundary layers relative to the electrode characteristic length at moderate scan rates such that steady-state conditions can be accessed as described for a disk electrode by Equation (3).[33]

$$I_{SS} = \pm 4nFDrC \tag{3}$$

I_{SS} (A) is the steady-state current and r (cm) is the microelectrode radius. As such, this technique is used to characterize the final SoC of the redox electrolyte (Figure S17), which can be calculated as a ratio of the oxidized current plateau to the sum of the oxidized and reduced current plateaus, accounting for differences in diffusion:

$$\mathrm{SoC} = \frac{C_O}{C_O + C_R} = \left(\frac{I_{ss,O}}{D_O}\right) / \left(\frac{I_{ss,O}}{D_O} + \frac{I_{ss,R}}{D_R}\right) \tag{4}$$

where the subscript "O" denotes the oxidized species and the subscript "R" denotes the reduced species. Note that we assume that the diffusion coefficient is unchanged with concentration such that the values shown in Figure 3 apply here. A final SoC of 50% would suggest that either no decay occurred or that the oxidized and reduced species decayed at equal rates–we estimate the final SoCs for the monomer, dimer, trimer, and tetramer as 44%, 46%, 44%, and 39%, respectively (Table 1). This reduction in SoC indicates a lower concentration of oxidized species as compared to reduced species, suggesting that the oxidized species has decayed or self-discharged more rapidly than the reduced species. Relative decay rates and pathways (e.g., self-discharge vs. decomposition) can also be evaluated via this method by extracting the oxidized and reduced species concentrations and comparing those to the starting cycling solution concentration. We find that the total decay determined via summation of estimated oxidized and reduced species concentrations and that of the cycling analysis are in reasonable agreement (Table 1); however, we also note that propagation of uncertainty in the diffusion coefficients can strongly influence these results, especially for the trimer where the relative uncertainty in the diffusion coefficients is largest (Table S8). Furthermore, the cycling duration, which influences the total decay sustained during the experiments, is dependent on the accessible capacity for each species (Figure 5) and is a convoluting factor in the final concentrations.

Table 1. State of charge (SoC) and species concentration for cycled solutions of the monomer and oligomers.

Species	Final (Initial) SoC [%]	Estimated final (initial) species concentration [mM]
Monomer	44 (50)	81.1 (100)
Dimer	46 (50)	44.8 (50)
Trimer	44 (50)	30.2 (33.3)
Tetramer	39 (50)	19.6 (25)

While microelectrode voltammetry is useful for ascertaining electrolyte SoC, macroelectrode voltammetry can offer complementary information regarding the presence of any electroactive decay species whose redox event occurs within the electrochemical window of interest. Figure 6 shows the post-cycling cyclic voltammograms for the monomer and each of the oligomer species, where the electrochemical window spans that accessed during cell cycling, and the solutions are again based on equivalent charge concentration such that differences in peak heights are related only to diffusivities. In the case of the monomer and dimer, minor peaks in the voltammogram suggest the presence of additional electroactive species, with new oxidation and reduction features emerging at potentials more positive than that of the TEMPO redox couple. In the case of the monomer, this redox event appears to be chemically irreversible, whereas there is a greater extent of reversibility for the dimer. The trimer and tetramer demonstrate somewhat similar behavior to the dimer but to a lesser extent. As the relative size of the decay peak seems to decrease with increasing size of oligomer, it is possible that the production of this decay species is hindered by the steric bulk of the oligomeric backbone; however, this trend may be obfuscated by the general reduction in currents and lower molecular concentration in this order of active species. While beyond the scope of this work, additional studies could help to shed light on the mechanistic nature and chemical identity of decay products such that recommenda-

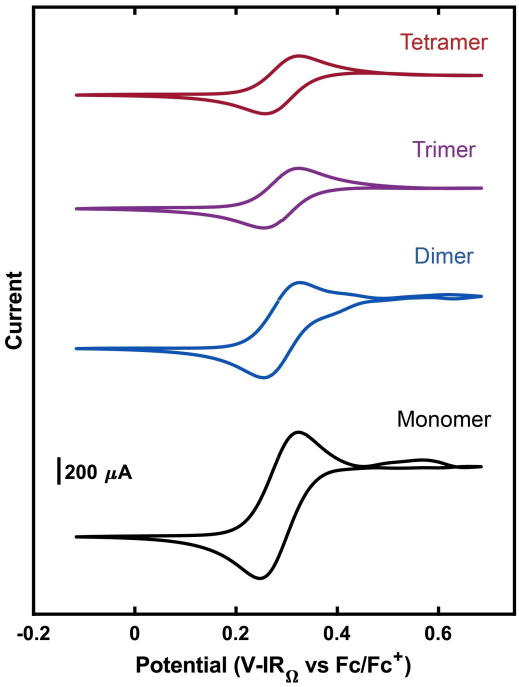

Figure 6. IR-corrected cyclic voltammograms of the cycled solutions using a 3-mm glassy carbon working electrode, a platinum wire counter electrode, and a Ag/Ag$^+$ reference electrode at 50 mV s^{-1}. Potentials are referenced against the Fc/Fc$^+$ redox couple. Prior to cycling, the solutions were composed of 100 mM charge concentration of each species deterministically prepared at 50% SoC with 0.5 M $TEABF_4$ in acetonitrile.

tions can be made for future molecular engineering of these oligomers.

Conclusions

In this work, we describe the relationship between the degree of oligomerization and the electrochemical and mass transport properties for a model system. Voltammetric characterization demonstrates that oligomerization of the TEMPO moiety to PEG-type backbones does not measurably influence the electrochemical reversibility of the redox reaction but does reduce the diffusion coefficients, albeit by less than one order of magnitude in all cases. In general, these results trend with increasing molecule size, though surprisingly the trimer rather than the tetramer displays the slowest diffusion. While metadynamics simulations imply that backbone flexibility contributes to this observation, further investigation is necessary to comprehensively elucidate the impact of different chain lengths on the solvation shell and its corresponding role. Subsequent EIS and polarization measurements in a symmetric cell configuration substantiate the ex situ electrochemical experiments–namely, we observe similar reaction kinetics and reduced mass transfer rates with oligomerization. Galvanostatic cell cycling also shows accessible capacities that align with these findings, and overall capacity fade rates were similar across all species. Decay was further evaluated with post-mortem voltammetric analyses, corroborating the decay rates according to the final SoC and elucidating the presence of some electroactive decay products at potentials positive of the TEMPO redox couple. Though the durational performance of the oligomers detailed here are likely not suitable for use in practical applications, the principles for functionalization and testing can be applied to other molecules with improved stability or extended to electrolyte systems at higher concentrations. We emphasize that caution must be exercised when engineering novel species, as this work has illustrated that certain combinations of oligomer scaffolds, redox-active centers, and electrolytes can impart nonobvious trends in molecular properties. Ultimately, utilization of such active species in this framework could help demonstrate oligomerization as a viable technique for improving long-term RFB performance.

Experimental Section

Voltammetry measurements

All materials were used as received. Macroelectrode voltammetry was collected using a 3-mm diameter glassy carbon disk electrode (BASi) with a platinum wire counter (BASi) and Ag/Ag^+ reference electrode (BASi, MF-2062) in 25 mL of 1 mM active species. Note that active species concentration denotes the oligomer rather than the active site (TEMPO moiety). TEMPO free radical (98%, Sigma Aldrich) was used as-received, and the oligomers were synthesized according to Section S1. The reference electrode was prepared by first dissolving 50 mM $AgBF_4$ ($\geq$99.99%, Sigma Aldrich) and 0.5 M $TEABF_4$ (>99.9%, Gotion) in acetonitrile ($\geq$99.9%, Sigma Aldrich). The solution was added to a fritted tube, sealed with a silver wire, and the resulting electrode was soaked in the same solution as its fill. Rotating disk electrode (RDE) voltammetry was collected using a 5-mm diameter glassy carbon disk electrode (Pine Research) on a Pine Instruments CPR rotator in 25 mL of 1 mM active species. Microelectrode voltammetry was collected using a 25-μm diameter Au disk electrode (BASi). All voltammetry measurements were conducted with 0.5 M $TEABF_4$ in acetonitrile. Prior to use, electrodes were polished on a MicroCloth pad containing an aqueous slurry of 0.05 μm alumina powder (Buehler Ltd.), rinsed with deionized water (18.2 MΩ cm, Milli-Q), dried with compressed air, and wiped with lens paper. All voltammetry measurements were conducted in an argon-filled glovebox (MBraun Labmaster, <1 ppm H_2O, <1 ppm O_2) at ca. 26 °C.

All macroelectrode voltammetry and RDE measurements were performed using a BioLogic VSP potentiostat, and these experiments were conducted in duplicate. Measurements were recorded with 85% IR-correction based on the impedance measured at 75 kHz (BioLogic ZIR technique). The 85% IR-correction is standard for cyclic voltammetry measurements, and the additional 15% manual IR-correction was neglected as it would not influence the results in any meaningful way at the cell resistance and current amplitudes recorded (i.e., the correction to all data points would be no more than 2.5 mV in all experiments). Cyclic voltammograms using the macroelectrode were performed for the following scan rates: 10, 20, 50, 100, 200, 500 $mV\,s^{-1}$. Peak currents (I_p) were background corrected over the first 100 mV of the scan window and calculated via the EC-Lab® Peak Analysis tool. The width at half maximum of the forward scan ($E_{p/2}$) and peak splitting (ΔE_p) were also determined using the EC-Lab® Peak Analysis tool. RDE voltammograms were collected at 10 $mV\,s^{-1}$. Plateau, or limiting, currents were similarly corrected over the first 100 mV of the scan window and calculated via the EC-Lab® Wave Analysis tool. All microelectrode voltammetry measurements were performed using a CH Instruments 630E potentiostat. Plateau, or limiting, currents were collected over data points 50–100 from the beginning and end of the initial sweep–this corresponds to a window of 50 mV. Referencing to the ferrocene couple was performed upon completion of each experiment by adding ca. 1 mM ferrocene to the solution, conducting scans at 50 $mV\,s^{-1}$, and determining the resulting redox potential relative to the reference. Redox (half-wave) potentials ($E_{1/2}$) were calculated as the mean potential between the forward and reverse CV peaks.

Metadynamics simulations

All simulations discussed herein were conducted using the CREST software package. Oligomers were first built in Avogadro, and the structure was optimized using the MMFF94 s force field to return bonds lengths and angles similar to those previously reported in the literature for PEG and TEMPO.[40,55] These oligomers were used as input structures into CREST (Figure S11). Due to the high degree of flexibility of the polymer backbone, simulations were found to be intractable on a standard laptop and instead were performed on the MIT SuperCloud[56]–even still, certain simulations, especially those for the tetramer remained intractable. Simulations that were predicted to last longer than five days were run using the built-in CREST "squick" command that runs the simulation at reduced settings. Reduced forms of the oligomers were simulated utilizing the "uhf" command to account for the radical centers, while oxidized forms were simulated using the "chrg" command. Simulations were conducted with the GFN2 level of theory with the xTB force field, and implicit solvation was performed using the analytical linearized Poisson-Boltzmann model. The conformational ensemble within 5 kcal mol^{-1} was obtained for the dimer, trimer with 2 repeat units, trimer with 3 repeat units, tetramer with 3

repeat units, and tetramer with 4 repeat units for the reduced and oxidized states in vacuum and implicit solvent acetonitrile. The radius of gyration was then calculated for each conformational state within the ensemble using the set of optimal conformations visualized in Avogadro (Figure S12).

Flow cell testing

All materials were used as received. Flow cell studies were conducted in a custom-built 2.55 cm^2 redox flow cell consisting of pristine SGL 29AA electrodes (Fuel Cell Store), interdigitated flow fields (IDFF), and a microporous Daramic 175 (175 μm nominal thickness, Daramic LLC) membrane.[57] The cell was constructed by stacking 2 electrodes on either side and using 2×GORE® Joint Sealant (10 mils, GORE®) gaskets such that a final compression of ca. 20% was achieved. 20 mL of electrolyte was deterministically prepared at 50% SoC by dissolving 50 mM TEMPO and 50 mM oxidized TEMPO, corresponding to a total charge concentration of 100 mM, with 0.5 M $TEABF_4$ in acetonitrile. The total charge concentration of 100 mM corresponds to active species concentrations of 50 mM, 33.3 mM, and 25 mM for the dimer, trimer, and tetramer, respectively. The electrolyte was distributed equally between two 10 mL Savillex jars, which served as electrolyte reservoirs, and flowed through Norprene tubing (Masterflex, L/S 16) joined to PFA tubing (Versilon, 1/8" ID) into the cell at 10 mL min^{-1} via a peristaltic pump (Masterflex L/S Series). All flow cell tests were conducted in an argon-filled glovebox (Inert Technologies, <1 ppm H_2O, <1 ppm O_2) at ca. 26 °C. All cells were pre-conditioned by flowing electrolyte through the electrodes at 10 mL min^{-1} for 1 h before data collection.

Data was collected in the order of EIS, polarization, and galvanostatic cell cycling using a BioLogic VSP potentiostat. EIS was performed in duplicate before proceeding to polarization. Measurements were taken about open circuit voltage, with an amplitude of 10 mV and a frequency range from 200 kHz to 10 mHz, averaging 6 points per decade and 5 measures per frequency recorded. The equivalent circuit fitting was conducted using the EC-Lab® Z Fit program. Polarization and cell cycling measurements were then recorded with 100% IR-correction based on the impedance measured at 100 kHz (BioLogic ZIR technique). Polarization measurements were recorded between ±0.5 V by galvanostatic holds of 60 s, recording one data point per second. Current densities were stepped in 5 mA cm^{-2} increments based on the geometric electrode area of 2.55 cm^2, which continued until the voltage cutoffs were reached in less than 60 s. The average voltage at a given current density was calculated from the last 50% of collected points to approximate steady state conditions. Cell cycling was then performed at 10 mA cm^{-2} with voltage cutoffs of ±0.5 V for 100 cycles. Post mortem analysis was conducted by removing the electrolyte from both compartments of the symmetric flow cell, mixing them together, and proceeding with the voltammetry procedures outlined above in "Voltammetry measurements."

CRediT authorship contribution statement

Trent A. Weiss: Conceptualization, Methodology, Validation, Investigation, Data curation, Visualization, Writing – original draft, Writing – review and editing. **Gang Fan**: Methodology, Validation, Data Curation, Visualization, Writing – original draft, Writing – review and editing. **Bertrand J. Neyhouse**: Conceptualization, Methodology, Validation, Investigation, Visualization, Supervision, Writing – original draft, Writing – review and editing. **Evan B. Moore**: Methodology, Data Curation. **Ariel Furst**: Project administration, Supervision, Writing – review and editing. **Fikile R. Brushett**: Conceptualization, Project administration, Supervision, Writing – original draft, Writing – review and editing.

Acknowledgements

This work was supported as part of the Joint Center for Energy Storage Research, an Energy Innovation Hub funded by the U.S. Department of Energy, Office of Science, Basic Energy Sciences. B.J.N gratefully acknowledges the NSF Graduate Research Fellowship Program under Grant Number 1122374. Any opinion, findings, and conclusions or recommendations expressed in this material are those of the authors and do not necessarily reflect the views of the NSF. We thank Dr. Jeffrey Kowalski and Dr. Katharine Greco of the Brushett Group as well as Dr. Yu Cao and Prof. Jeffrey Moore at the University of Illinois at Urbana-Champaign for their contributions to conceptualizing the framework and to preliminary testing for this study. We also thank Dr. Clorice Reinhardt of the Kulik Group, Chinmay Gangul of the Rutledge Group, and Dr. Aditya Limaye of Tyba Energy for their advice and guidance in performing the metadynamics simulations. The authors acknowledge the MIT SuperCloud and Lincoln Laboratory Supercomputing Center for providing HPC resources that have contributed to the research results reported within this manuscript.

Conflict of Interests

The authors declare no conflict of interest.

Data Availability Statement

The data that support the findings of this study are available from the corresponding author upon reasonable request.

Keywords: cyclic voltammetry · electrochemistry · oligomerization · redox flow battery · TEMPO

[1] S. Chu, A. Majumdar, *Nature* **2012**, *488*, 294–303.
[2] B. R. Chalamala, T. Soundappan, G. R. Fisher, M. R. Anstey, V. V. Viswanathan, M. L. Perry, *Proc. IEEE* **2014**, *102*, 976–999.
[3] K. E. Rodby, T. J. Carney, Y. Ashraf Gandomi, J. L. Barton, R. M. Darling, F. R. Brushett, *J. Power Sources* **2020**, *460*, 227958.
[4] Y. Ding, C. Zhang, L. Zhang, Y. Zhou, G. Yu, *Chem. Soc. Rev.* **2018**, *47*, 69–103.
[5] J. Yuan, Z.-Z. Pan, Y. Jin, Q. Qiu, C. Zhang, Y. Zhao, Y. Li, *J. Power Sources* **2021**, *500*, 229983.
[6] M. Li, Z. Rhodes, J. R. Cabrera-Pardo, S. D. Minteer, *Sustain. Energy Fuels* **2020**, *4*, 4370–4389.
[7] M. L. Perry, J. D. Saraidaridis, R. M. Darling, *Curr. Opin. Electrochem.* **2020**, *21*, 311–318.
[8] R. Darling, K. Gallagher, W. Xie, L. Su, F. Brushett, *J. Electrochem. Soc.* **2016**, *163*, A5029–A5040.
[9] C. R. Peltier, Z. Rhodes, A. J. Macbeth, A. Milam, E. Carroll, G. W. Coates, S. D. Minteer, *ACS Energy Lett.* **2022**, *7*, 4118–4128.
[10] E. C. Montoto, G. Nagarjuna, J. S. Moore, J. Rodríguez-López, *J. Electrochem. Soc.* **2017**, *164*, A1688–A1694.

[11] S. E. Doris, A. L. Ward, A. Baskin, P. D. Frischmann, N. Gavvalapalli, E. Chénard, C. S. Sevov, D. Prendergast, J. S. Moore, B. A. Helms, *Angew. Chem. Int. Ed.* **2017**, *56*, 1595–1599.
[12] M. Burgess, J. S. Moore, J. Rodríguez-López, *Acc. Chem. Res.* **2016**, *49*, 2649–2657.
[13] E. C. Montoto, G. Nagarjuna, J. Hui, M. Burgess, N. M. Sekerak, K. Hernández-Burgos, T.-S. Wei, M. Kneer, J. Grolman, K. J. Cheng, J. A. Lewis, J. S. Moore, J. Rodríguez-López, *J. Am. Chem. Soc.* **2016**, *138*, 13230–13237.
[14] M. J. Baran, M. N. Braten, E. C. Montoto, Z. T. Gossage, L. Ma, E. Chénard, J. S. Moore, J. Rodríguez-López, B. A. Helms, *Chem. Mater.* **2018**, *30*, 3861–3866.
[15] K. H. Hendriks, S. G. Robinson, M. N. Braten, C. S. Sevov, B. A. Helms, M. S. Sigman, S. D. Minteer, M. S. Sanford, *ACS Cent. Sci.* **2018**, *4*, 189–196.
[16] M. Burgess, K. Hernández-Burgos, J. K. Schuh, J. Davila, E. C. Montoto, R. H. Ewoldt, J. Rodríguez-López, *J. Am. Chem. Soc.* **2018**, *140*, 2093–2104.
[17] M. Milton, Q. Cheng, Y. Yang, C. Nuckolls, R. Hernández Sánchez, T. J. Sisto, *Nano Lett.* **2017**, *17*, 7859–7863.
[18] S. Odom, *ACS Cent. Sci.* **2018**, *4*, 140–141.
[19] Z. T. Gossage, K. Hernández-Burgos, J. S. Moore, J. Rodríguez-López, *ChemElectroChem* **2018**, *5*, 3006–3013.
[20] N. Gavvalapalli, J. Hui, K. J. Cheng, T. Lichtenstein, M. Shen, J. S. Moore, J. Rodríguez-López, *J. Am. Chem. Soc.* **2014**, *136*, 16309–16316.
[21] M. Burgess, K. Hernández-Burgos, B. H. Simpson, T. Lichtenstein, S. Avetian, G. Nagarjuna, K. J. Cheng, J. S. Moore, J. Rodríguez-López, *J. Electrochem. Soc.* **2016**, *163*, H3006–H3013.
[22] V. A. Iyer, J. K. Schuh, E. C. Montoto, V. P. Nemani, S. Qian, G. Nagarjuna, J. Rodríguez-López, R. H. Ewoldt, K. C. Smith, *J. Power Sources* **2017**, *361*, 334–344.
[23] G. Nagarjuna, J. Hui, K. J. Cheng, T. Lichtenstein, M. Shen, J. S. Moore, J. Rodríguez-López, *J. Am. Chem. Soc.* **2014**, *136*, 16309–16316.
[24] M. J. Baran, M. N. Braten, S. Sahu, A. Baskin, S. M. Meckler, L. Li, L. Maserati, M. E. Carrington, Y.-M. Chiang, D. Prendergast, B. A. Helms, *Joule* **2019**, 2968–2985.
[25] M. J. Baran, M. E. Carrington, S. Sahu, A. Baskin, J. Song, M. A. Baird, K. S. Han, K. T. Mueller, S. J. Teat, S. M. Meckler, C. Fu, D. Prendergast, B. A. Helms, *Nature* **2021**, *592*, 225–231.
[26] A. Shrestha, K. H. Hendriks, M. S. Sigman, S. D. Minteer, M. S. Sanford, *Chem. Eur. J.* **2020**, *26*, 5369–5373.
[27] J. D. Milshtein, J. L. Barton, R. M. Darling, F. R. Brushett, *J. Power Sources* **2016**, *327*, 151–159.
[28] J. E. Nutting, M. Rafiee, S. S. Stahl, *Chem. Rev.* **2018**, *118*, 4834–4885.
[29] N. H. Attanayake, Z. Liang, Y. Wang, A. P. Kaur, S. R. Parkin, J. K. Mobley, R. H. Ewoldt, J. Landon, S. A. Odom, *Mater Adv* **2021**, *2*, 1390–1401.
[30] Y. Zhao, J. Zhang, G. Agarwal, Z. Yu, R. E. Corman, Y. Wang, L. A. Robertson, Z. Shi, H. A. Doan, R. H. Ewoldt, I. A. Shkrob, R. S. Assary, L. Cheng, V. Srinivasan, S. J. Babinec, L. Zhang, *J. Mater. Chem. A* **2021**, *9*, 16769–16775.
[31] N. G. Connelly, W. E. Geiger, *Chem. Rev.* **1996**, *96*, 877–910.
[32] R. S. Nicholson, Irving Shain, *Anal. Chem.* **1964**, *36*, 706–723.
[33] A. J. Bard, L. R. Faulkner, *Electrochemical Methods: Fundamentals and Applications 2nd ed.*, Wiley, **2000**, pp. 156–260.
[34] J. B. Flanagan, S. Margel, A. J. Bard, F. C. Anson, *J. Am. Chem. Soc.* **1978**, *100*, 4248–4253.
[35] Z. Li, S. Li, S. Liu, K. Huang, D. Fang, F. Wang, S. Peng, *Electrochem. Solid-State Lett.* **2011**, *14*, A171.
[36] T. Suga, Y.-J. Pu, K. Oyaizu, H. Nishide, *BCSJ* **2004**, *77*, 2203–2204.
[37] R. Berthin, A. Serva, K. G. Reeves, E. Heid, C. Schröder, M. Salanne, *J. Chem. Phys.* **2021**, *155*, 074504.
[38] J. Andrews, E. Blaisten-Barojas, *J. Phys. Chem. B* **2019**, *123*, 10233–10244.
[39] S. Hezaveh, S. Samanta, G. Milano, D. Roccatano, *J. Chem. Phys.* **2012**, *136*, 124901.
[40] H. Lee, R. M. Venable, A. D. MacKerell, R. W. Pastor, *Biophys. J.* **2008**, *95*, 1590–1599.
[41] D. Dhabal, Z. Jiang, A. Pallath, A. J. Patel, *J. Phys. Chem. B* **2021**, *125*, 5434–5442.
[42] J. E. Mark, *Physical Properties of Polymers Handbook 2nd ed.*, Springer, New York, **2007**, pp. 43–57 and 447–454.
[43] C. W. Nyambura, J. Sampath, E. Nance, J. Pfaendtner, *J. Appl. Polym. Sci.* **2022**, *139*, e52732.
[44] P. Pracht, F. Bohle, S. Grimme, *Phys. Chem. Chem. Phys.* **2020**, *22*, 7169–7192.
[45] S. Grimme, *J. Chem. Theory Comput.* **2019**, *15*, 2847–2862.
[46] B. J. Neyhouse, J. Lee, F. R. Brushett, *J. Electrochem. Soc.* **2022**, *169*, 090503.
[47] J. L. Barton, J. D. Milshtein, J. J. Hinricher, F. R. Brushett, *J. Power Sources* **2018**, *399*, 133–143.
[48] S. K. Murthy, A. K. Sharma, C. Choo, E. Birgersson, *J. Electrochem. Soc.* **2018**, *165*, A1746.
[49] G. Paasch, K. Micka, P. Gersdorf, *Electrochim. Acta* **1993**, *38*, 2653–2662.
[50] X.-Z. Yuan, C. Song, H. Wang, J. Zhang, in *Electrochemical Impedance Spectroscopy in PEM Fuel Cells: Fundamentals and Applications*, Springer, London, **2010**, pp. 139–192.
[51] D. G. Kwabi, Y. Ji, M. J. Aziz, *Chem. Rev.* **2020**, *120*, 6467–6489.
[52] M.-A. Goulet, M. J. Aziz, *J. Electrochem. Soc.* **2018**, *165*, A1466.
[53] B. Ok, W. Na, T.-H. Kwon, Y.-W. Kwon, S. Cho, S. M. Hong, A. S. Lee, J. H. Lee, C. M. Koo, *J. Ind. Eng. Chem.* **2019**, *80*, 545–550.
[54] I. A. Volodin, C. Stolze, O. Nolte, P. Rohland, M. D. Hager, U. S. Schubert, *ACS Appl. Energ. Mater.* **2023**, *6*, 302–316.
[55] A. Abe, J. E. Mark, *J. Am. Chem. Soc.* **1976**, *98*, 6468–6476.
[56] A. Reuther, J. Kepner, C. Byun, S. Samsi, W. Arcand, D. Bestor, B. Bergeron, V. Gadepally, M. Houle, M. Hubbell, M. Jones, A. Klein, L. Milechin, J. Mullen, A. Prout, A. Rosa, C. Yee, P. Michaleas, *in 2018 IEEE High Performance Extreme Computing Conference (HPEC)* **2018**, pp. 1–6.
[57] J. D. Milshtein, A. P. Kaur, M. D. Casselman, J. A. Kowalski, S. Modekrutti, P. L. Zhang, N. H. Attanayake, C. F. Elliott, S. R. Parkin, C. Risko, F. R. Brushett, S. A. Odom, *Energy Environ. Sci.* **2016**, *9*, 3531–3543.

Manuscript received: January 31, 2023
Revised manuscript received: June 8, 2023
Accepted manuscript online: June 15, 2023
Version of record online: July 20, 2023